SiGe quantum well infrared photodetectors on strained-silicon-on-insulator

JOHANNES ABERL,[1] MORITZ BREHM,[1] THOMAS FROMHERZ,[1] JEFFREY SCHUSTER,[1] JACOPO FRIGERIO,[2] AND PATRICK RAUTER[1,*]

[1]*Institute of Semiconductor and Solid State Physics, Johannes Kepler University Linz, Altenberger Straße 69, A-4040 Linz, Austria*
[2]*L-NESS, Dipartimento di Fisica del Politecnico di Milano, Polo Territoriale di Como, Via Anzani 42, Como I-22100, Italy*
*patrick.rauter@jku.at

Abstract: We demonstrate p-type SiGe quantum well infrared photodetectors (QWIPs) on a strained-silicon-on-insulator (sSOI) substrate. The sSOI system allows strain-balancing between the QWIP heterostructure with an average composition of $Si_{0.7}Ge_{0.3}$ and the substrate, and therefore lifts restrictions to the active material thickness faced by SiGe growth on silicon or silicon-on-insulator substrates. The realized sSOI QWIPs feature a responsivity peak at detection wavelengths around 6 μm, based on a transition between heavy-hole states. The fabricated devices have been thoroughly characterized and compared to equivalent material simultaneously grown on virtual $Si_{0.7}Ge_{0.3}$ substrates based on graded SiGe buffers. Responsivities of up to 3.6 mA/W are achieved by the sSOI QWIPs at 77 K, demonstrating the large potential of sSOI-based devices as components for a group-IV optoelectronic platform in the mid-infrared spectral region.

1. Introduction

With the prospect of compact, robust and cheap integrated sensing and detection systems, the development of an optoelectronic group-IV-based platform for monolithic integration on a multi-functional chip continues to draw comprehensive research interest. And while work on silicon-based components for increased optical data transfer rates focuses on the telecommunication wavelength range [1–10], efforts towards an integrated sensing platform for novel lab-on-a-chip solutions target the mid-infrared regime [11–15]. The latter is a well-known spectral fingerprint region including the vibrational and rotational absorption lines used to unambiguously identify chemical compounds. Among the demonstrated group-IV building blocks for such a mid-infrared platform are quantum well infrared photodetectors (QWIPs) [16–19], quantum cascade (QC) emitters [20,21], silicon-on-insulator (SOI) based waveguides [22], Ge waveguides on SiN [23], SiGe waveguides [24], SiGe polarization rotators [25] and Ge-based multiplexers [26]. One of the fundamental challenges faced by SiGe-based platform components is the lattice mismatch between Si and Ge. On conventional Si substrates, the composition range and stack thickness accessible for monolithic compound structures pseudomorphically grown in epitaxial systems is crucially limited due to the accumulation of strain and the associated formation of defects. In an approach to overcome this difficulty, virtual substrates with a Ge content matched to the average composition of the active structure enables growth of arbitrarily thick material [21,27]. In recent years, the buffer thickness required for high-quality virtual substrates with low surface defect densities has been gradually reduced through elaborate growth schemes down to state-of-the-art values around 1 μm [28]. Another recently reported approach comprises growth of SiGe QWIPs on relaxed nanomembrane templates of the same heterostructure, providing intrinsic strain-balancing between substrate and grown material [17]. A highly promising alternative

to conventional Si and virtual SiGe substrates is presented by strained-silicon-on-insulator (sSOI) technology [29], which allows strain-balanced growth on only a few nanometers thick device layers. However, the use of sSOI substrates for group-IV photonics remains largely unexplored and up to now no mid-infrared devices have been realized on sSOI. In this work, we demonstrate a p-type SiGe QWIP on sSOI. The optically active material is strain-balanced to the sSOI substrate with a device layer strained to the in-plane lattice constant of relaxed $Si_{0.7}Ge_{0.3}$ and operates in the wavelength regime around 6 μm. The thin buried oxide layer of the substrate (thickness around 130 nm) enables competitive detector operation even at these large wavelengths despite the strong absorption of silicon oxide in this region. The devices were thoroughly characterized and compared to material simultaneously grown on conventional virtual substrates, demonstrating both excellent agreement between the QWIP bandstructure design and the responsivity characteristics as well as the superior performance of the sSOI devices as compared to those grown on a virtual substrate.

2. Material growth and x-ray characterization

The studied p-type QWIP material was grown by MBE in a Riber SIVA45 solid-source system. Growth was performed simultaneously on an sSOI substrate provided by SOITEC and a virtual $Si_{0.7}Ge_{0.3}$ substrate fabricated by the group of G. Isella, both in [100] orientation. The virtual substrate is formed by 2 μm of fully relaxed $Si_{0.7}Ge_{0.3}$ on top of a 4-μm-thick graded SiGe buffer, both grown on a Si wafer by low energy plasma enhanced chemical vapor deposition (LEPECVD) [30]. The buffer was deposited at a rate of 5-10 nm/s, where the Ge concentration was gradually increased from 0% to 30% at a rate of 7% per μm. The sSOI substrate features a 30-nm-thick sSOI device layer on roughly 130 nm of buried oxide. The thin device layer exhibits an in-plane lattice constant equivalent to that of relaxed $Si_{0.7}Ge_{0.3}$ and therefore provides growth conditions equivalent to the virtual substrate. Initially, 300 nm of $Si_{0.7}Ge_{0.3}$ were grown as a bottom contact layer, boron doped at a density of $2 \cdot 10^{18}$ cm^{-3}. The active region itself comprises ten quantum wells formed by nominally 2.3 nm of $Si_{0.38}Ge_{0.62}$ and separated by $Si_{0.74}Ge_{0.26}$ barriers of 18.4 nm width. A 7-nm-wide region of each barrier layer was boron doped at a concentration of $5 \cdot 10^{17}$ cm^{-3}, set back from the nearest quantum well by 2.2 nm and separated from the other neighboring well by 9.2 nm. The modulation doping is therefore asymmetric, and the doped region is closer to the earlier grown of two neighboring quantum wells. As a final growth step, 100 nm of $Si_{0.74}Ge_{0.26}$ were grown as a top contact layer, again boron doped at $2 \cdot 10^{18}$ cm^{-3}. Both the first and the last quantum well of the active region are separated from the highly doped contact layers by 18.4 nm of $Si_{0.74}Ge_{0.26}$ barrier material. Schematics of the material layout are shown in Figs. 1(a) and 1(b) for the sSOI and virtual substrates, respectively.

The material was structurally characterized by high-resolution x-ray diffraction measurements, where Figs. 1(c) and 1(d) present reciprocal space maps acquired for QWIP material grown on sSOI and virtual substrate, respectively. For both material chips, the periodic superlattice peaks in the asymmetric (224) map confirm pseudomorphic growth: An evaluation of the central superlattice peak position gives in-plane lattice constants of 5.494 Å and 5.493 Å for the material on sSOI and virtual substrate, respectively, equivalent to those of relaxed $Si_{0.697}Ge_{0.303}$ and $Si_{0.701}Ge_{0.299}$. The theoretical lattice constant of relaxed $Si_{0.7}Ge_{0.3}$ at room temperature is 5.4934 Å [31]. Note the broad contribution by the graded SiGe buffer of the virtual substrate in the maps of Fig. 1(d), stretching between the Si and superlattice peaks. As expected, this feature is absent from Fig. 1(c), where the contribution by the sSOI device layer coincides with the central superlattice peak. As indicated by the non-zero Q_y-value of the silicon bulk reflex in the (004) map of Fig. 1(c), the crystal structure of the sSOI device layer on top of the buried oxide and of the grown heterostructure is slightly tilted in respect to that of the substrate handling wafer. A comparison between the diffraction peak broadening in Figs. 1(c) and 1(d) suggests a superior structural quality of the material grown on the sSOI substrate, as the respective reflections are

considerably sharper than those recorded for the virtual substrate material. The detailed nature of the structural difference between the two is difficult to ascertain within the scope of this publication. A probable cause for diffraction peak broadening in Q_y direction is the presence of threading dislocations [32,33], hinting at a possibly higher threading dislocation density of the virtual substrate material as compared to that grown on sSOI. As discussed later on, the higher structural quality of the latter is reflected in a superior device performance in comparison to the former. Figure 1(e) presents a line cut through the (004) map in Fig. 1(c), along with a model fit used to evaluate the actual material composition. The fit parameters suggest a composition of the quantum well and barrier layers of $Si_{0.373}Ge_{0.627}$ and $Si_{0.734}Ge_{0.266}$, respectively, very close to the nominal $Si_{0.38}Ge_{0.62}$ and $Si_{0.74}Ge_{0.26}$. Furthermore, the barrier thickness seems slightly decreased from the nominal 18.4 nm to 18.2 nm, which gives an actual average Ge content of the active material of 30.65% instead of the targeted 30%. The latter is well within the tolerance for relaxation-free growth, and the associated predicted changes in the QWIP bandstructure are
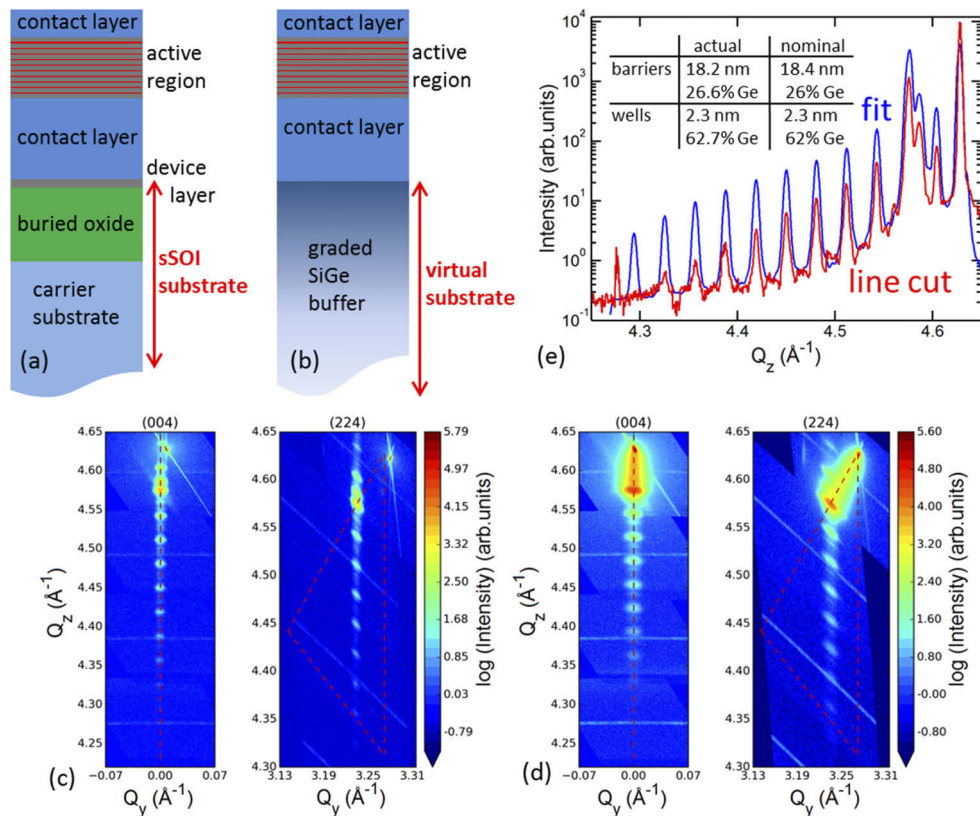

Fig. 1. Material layout and reciprocal space maps. (a) Schematics of the QWIP heterostructure stack grown on sSOI. (b) Analogue layout of the material on virtual substrate. (c) Diffracted x-ray intensity as a function of the scattering wave vector components around the (004) and (224) peaks of Si. Maps for the SiGe QWIP material grown on sSOI. (d) The respective data for the equivalent structure grown on virtual substrate. The asymmetric (224) maps indicate excellent pseudomorphic growth of the material with an in-plane lattice constant equivalent to relaxed $Si_{0.7}Ge_{0.3}$. Note the significantly narrower superlattice peaks for the sSOI material, suggesting a higher structural quality compared to the virtual substrate QWIP. (e) Line cut through the (004) map in Fig. 1(c) together with the simulated characteristics obtained for the fitted actual parameters shown in the table.

also too insignificant to influence the detector operation. Put differently, the QWIP material parameters match the design values with high accuracy, where the actual quantum well width and material composition fall within 1 Å and 1% of the design parameters, respectively.

3. Device fabrication and band structure

Following the x-ray characterization, the QWIP material was processed into mesa devices for biasing and charge transport along the growth direction, where standard Si processing technology and optical lithography were used for structural patterning. The device mesas were defined by dry-etching in SF_6 and O_2 masked by photoresist. 200 nm of AlSi metallization were applied to the highly doped top and bottom contact layers, allowing electrical contacting of the QWIP structure by Al wire bonding. The square-shaped mesa devices exhibit in-plane dimensions of 400 μm × 400 μm and a height of 380 nm, with a top surface completely covered by the AlSi top metallization. In order to facilitate illumination of the active region in waveguide geometry by linearly polarized radiation with an electric field component either in growth direction (transverse magnetic, TM) or parallel to the device surface (transverse electric, TE), the chip backside was polished and a facet angled at 30° to the surface was lapped into the chip sidewall. Figure 2(a) illustrates the device layout. The fully processed chips were mounted epilayer-up to chip carriers and built into a cryostat equipped with a ZnSe window for optoelectronic characterization at cryogenic temperatures. A temperature sensor (thermistor) was mounted on the heat sink close to the QWIP chip. As the power dissipated across the device is extremely low, the actual device temperature is expected to be well represented by the measured value.

The SiGe QWIPs demonstrated in this work are designed for the detection of TM polarized radiation based on an optical transition between confined heavy-hole (HH) states. The grown heterostructure forms quantum wells in the valence band due to a band discontinuity at the interface between $Si_{0.38}Ge_{0.62}$ and $Si_{0.74}Ge_{0.26}$. Figure 2(b) presents the simulated band structure of the fabricated active material according to a six-band k.p envelope function model based on a strain-dependent Luttinger-Kohn Hamiltonian as described in detail in Ref. [34]. The band edges were calculated self-consistently, including band bending due to the equilibrium distribution of charge carriers. For the presented simulation results, the actual material parameters obtained from the x-ray data were used rather than the nominal ones. However, changes in the bandstructure related to the difference between the nominal and actual parameter sets are insignificant in respect to the device operation. As seen in Fig. 2(b), the formed quantum wells feature a HH ground state due to the compressively strained well material. The QWIP design relies on an optical transition from this bound HH ground state (HH1) into HH states located slightly above the barrier band edge (dominantly HH2).

This kind of operation in the transition regime between a bound-to-bound and a bound-to-continuum design is a well-known QWIP concept commonly employed in n-type III-V systems [35]. The transition energy between HH1 and HH2 at vanishing in-plane wavevector is calculated as 168 meV. Charge carriers optically excited from the HH1 ground state into HH2 are accelerated by the electric field across the structure, escape the well region with a certain probability and generate a photocurrent, the strength of which in addition depends on the so-called photoconductive gain. (The detailed operation of QWIPs is well known and can be found in literature [35].) The sSOI QWIP is therefore expected to feature a responsivity peak around a photon energy of 168 meV, which is dominant for TM-polarized radiation, analogue to III-V QWIPs.
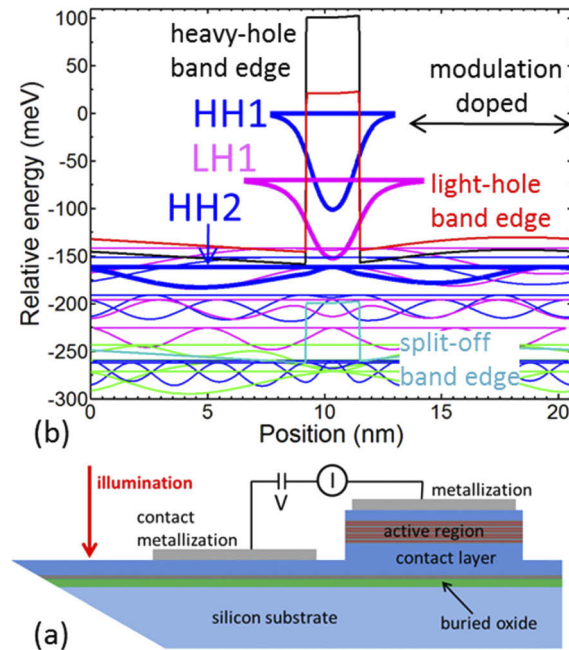
Fig. 2. (a) Device schematics of the sSOI QWIPs. A facet was lapped into the chip wall at an angle of 30° to the surface for illumination in waveguide geometry. (b) Valence band structure of one period of the SiGe QWIPs in absence of an external field. The valence band edges for the heavy-hole (HH), light-hole (LH) and split-off (SO) bands are presented. Note the band bending induced by the modulation doped barriers. The absolute square of the eigenfunctions calculated for vanishing in-plane wavevectors at their respective eigenenergy position are shown, where the states represented by blue, pink and green curves are dominantly composed of HH, LH and SO states, respectively. Eigenenergy values are given for electrons (hole energies are of opposite sign), relative to the HH1 ground state.

4. Spectral characterization of the SiGe QWIP responsivity

The spectrally resolved responsivity of the SiGe QWIPs was experimentally determined at a device temperature of 77 K. The fabricated devices were employed as detector element in a Fourier-transform infrared spectrometer (FTIR), and spectra of a globar source were recorded. For this purpose, the top contact of a QWIP mesa was biased in respect to the grounded bottom contact, and the resulting current was measured using a low-noise current preamplifier providing the detector signal input for the FTIR. The spectrometer radiation output was coupled into the angled SiGe chip facet, where a linear wire-grid polarizer in front of the latter enables device illumination in either TM or TE polarization. The device schematics are shown in Fig. 2(a) for the sSOI QWIP. The spectra recorded in fast-scan mode were normalized to a globar reference spectrum taking into account the transmission characteristics of all involved optical components in order to gain the QWIP responsivity characteristics. The responsivity spectra were finally calibrated by measuring the total current response of the devices to a commercial black-body source at a homogenous and precise temperature of 500°C.

Figure 3(a) presents the responsivity spectra for an sSOI QWIP at liquid-nitrogen temperature in dependence of the applied bias for TM (solid lines) and TE (broken lines) polarized radiation. The spectra are dominated by a prominent peak centered around a photon energy of 200 meV, which is strong in TM polarization only. The latter is expected for an intersubband transition between two HH states. Note that the position of the responsivity maximum is shifted by 30

meV from the value predicted by the simulations. The reason for this discrepancy is revealed by comparing the sSOI QWIP data to the responsivity obtained for the QWIP simultaneously grown on a virtual substrate. Figure 3(b) shows the data recorded for devices on both chips together with the respective simulated absorption spectra based on the bandstructure calculations. For the QWIP grown on a virtual substrate, the dominant responsivity peak is centered at a photon energy of 168 meV, which precisely matches the HH1-HH2 transition energy obtained from the bandstructure calculations. The measured spectral response of this device is therefore remarkably well reproduced by the simulated absorption spectra, where details on the calculation of the latter can be found in Ref. [34]. The virtual substrate device exhibits the slightly asymmetric spectral characteristics typical for QWIPs operating between the pure bound-to-bound and bound-to-continuum regimes. Now, the deviation of the sSOI QWIP spectra from both the simulated ones and those measured for the virtual substrate counterpart are clearly related to the singular crucial difference between the two substrate platforms, namely the buried oxide of the former. Due to the index contrast between the oxide and the active material a cavity is formed. As a consequence, cavity effects have to be expected, where the resonance positions depend on the exact coupling angle in waveguide geometry and the boundary conditions resulting from the top metallization and bottom dielectric interfaces. For the device geometry shown in Fig. 2(a), the incoming radiation is guided to the QWIP mesa at an angle of 30° to the chip surface. With a refractive index of around 3.4 and a thickness of the grown material of 623 nm, a simple estimate positions the first cavity resonance at roughly 8.5 μm (150 meV). Due to the high absorption coefficient of silicon oxide around 1000 cm^{-1} in this region [36], radiation confined to the mesa cavity experiences strong absorption losses, suppressing the device responsivity around 168 meV and shifting the spectral peak to 200 meV. The responsivity values obtained for the sSOI device are slightly higher than those of the virtual substrate counterpart, which is probably related to a difference in photoconductive gain between the devices, or again caused by cavity effects. In addition to the dominant responsivity peak in TM polarization, the spectra in Fig. 3(a) show a significantly broader response to TE polarized radiation at higher photon energies around 380 meV, which originates from transition into light-hole (LH) continuum states. Note that while the simulation data predict a very broad absorption peak for TE polarized radiation, the measured responsivity spectrum of the sSOI QWIP is more structured. Again, this is due to buried-oxide induced cavity effects. Furthermore, minor deviations between simulated absorption and measured responsivity at higher transition energies associated with final states high up in the continuum are common, particularly as the simulation does not consider the carrier transport properties relevant for the generation of photocurrent. The simulated absorption spectrum for TM polarized radiation further exhibits a side peak around 240 meV originating from a transition into split-off states (green curve in Fig. 2(b)), which is not observed in the experimental responsivity spectrum. The latter is probably due to the quasi-bound nature of the final split-off state.

Quantitatively, at 77 K the sSOI QWIP responsivity reaches values of 1.7 mA/W at zero-bias and increases steadily with the applied voltage up to 3.6 mA/W at a bias (field) of 0.5 V (24 kV/cm). The high responsivity at zero-bias relies on a built-in field originating from the asymmetric modulation doping of the QWIP barriers, as indicated by the band bending in the bandstructure plot in Fig. 2(b). As a consequence of this asymmetric doping, positive biasing of the devices is the optimal mode of operation for the demonstrated QWIPs. The broken line in Fig. 4(a) shows the total photocurrent density generated by a chopped black body radiator at 500°C measured in lock-in technique and used for the responsivity calibration. Note that the current values presented by the broken line therefore do not include the respective dark-current contributions. The data indicates that positive biasing favors higher photocurrents and that a photocurrent minimum is reached at -0.12 V, where the effect of the doping-induced built-in field mentioned above is compensated by the external bias. The responsivity values achieved by the sSOI QWIP compare well to those of SiGe QWIPs reported in literature: Already at zero-bias, the sSOI device reaches
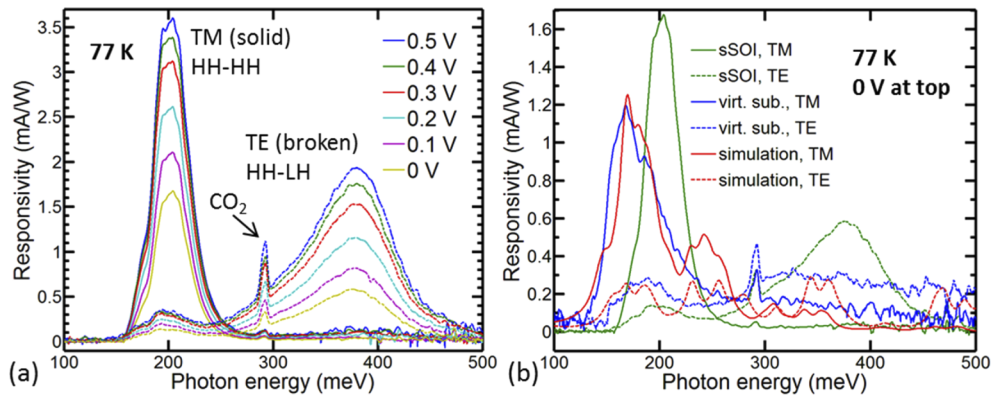
Fig. 3. SiGe QWIP responsivity spectra in polarization dependence of the incoming radiation at a device temperature of 77 K. (a) Bias-dependent responsivity characteristics of an sSOI QWIP. The dominant peak in TM polarization originates from a transition between the HH1 and HH2 states in Fig. 2(b). The component sensitive to TE polarized radiation results from transitions between HH1 and LH continuum states. Note that the narrow peak labelled CO_2 is a normalization artefact caused by the CO_2 absorption line in the photocurrent and globar source spectra. (b) Comparison between the responsivity characteristics of the sSOI QWIP with a device on virtual substrate, together with the simulated absorption spectra scaled to fit the latter. Note the excellent agreement between the simulated spectra and the responsivity of the virtual substrate QWIP. The shift of the responsivity peaks of the sSOI material is induced by the optical cavity formed by the buried oxide of the sSOI substrate.

peak responsivities significantly higher than any of the QWIPs previously reported by the authors, both on conventional Si substrates [16] and on virtual substrates [27,37].
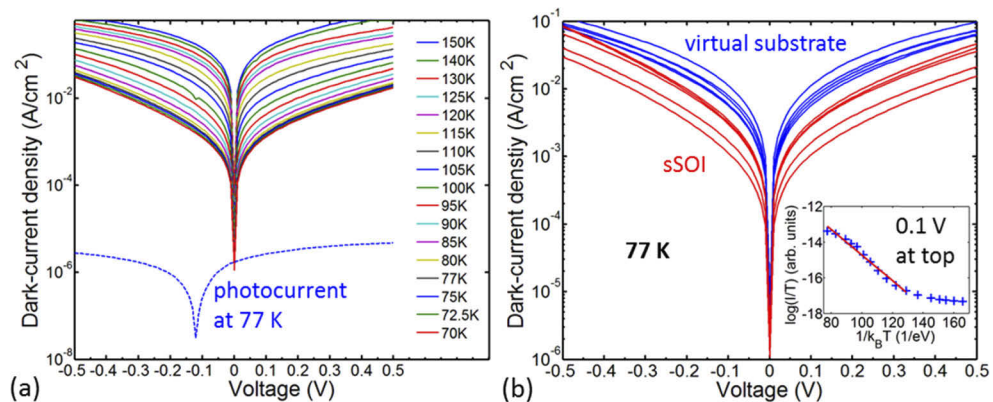

Fig. 4. SiGe QWIP dark-current characteristics. (a) Temperature dependence of the dark-current densities for an sSOI QWIP device, together with the total photocurrent response to a calibrated black-body source at 500°C (broken blue line) at 77 K. (b) Dark-current characteristics recorded for a series of devices on both the virtual substrate and sSOI based chips. The virtual substrate QWIPs exhibit significantly higher dark-currents, and the data suggests that the overall high dark-current is related to the substrate quality. The inset shows an Arrhenius plot of the data in Fig. 4(a) at a bias of 0.1 V together with a linear fit. The latter indicates an activation energy of 71 meV, which corresponds to the HH1-LH1 transition energy in Fig. 2(b).

5. Dark-current characteristics

Figure 4(a) shows the dark-current density characteristics of an sSOI QWIP for a series of temperatures between 70 K and 150 K, acquired by covering the cryostat window by a cooled shield. The observed dark-currents are very high compared to those reported in literature for other SiGe QWIP devices [16–18]. Densities rise above 1 mA/cm^2 already at voltages (fields) below 0.1V (5.8 kV/cm), and are for finite bias therefore two to three orders of magnitude higher than previously achieved for SiGe QWIPs. An evaluation of the temperature dependence of the dark-current characteristics allows an interpretation of the high observed current values. The inset of Fig. 4(b) presents an Arrhenius plot of the dark-current values recorded for an sSOI QWIP device at a bias of 0.1 V together with a linear fit of the high-temperature region (90 K and up). The fit suggests a dark-current activation energy of 71 meV, which is equivalent to the energetic spacing between the HH1 ground state and the lowest LH state (LH1) as calculated by our simulations and seen in Fig. 2(b). Therefore, at high temperatures the dark-current seems dominated by inter-well tunneling of charge carriers thermally excited into the LH1 state, indicating that the QWIP barrier thickness was chosen too small. However, the deviation of the dark-current characteristics from the linear behavior in the inset of Fig. 4(b) indicates additional contributions dominating the device current around 77 K, which do not originate from LH1 tunneling. This additional dark-current most likely originates from defect current channels through the barrier. A comparison between the dark-current characteristics of several devices on both the sSOI and the virtual substrate chips in Fig. 4(b) reveals that the QWIPs on the latter consistently suffer from higher dark-currents than those on sSOI. The indication of a lower structural quality of the virtual substrate material by the reciprocal space maps in Fig. 1(d) suggests that the higher dark-currents for these QWIPs are caused by substrate-related defect or threading dislocation channels. Thus, similar leakage current channels are most likely the cause for the significantly lower but still high dark-currents of the sSOI devices.

6. Discussion and conclusions

Despite the relatively high dark-currents at finite bias, the large responsivity observed at zero-bias nevertheless allows competitive operation of the sSOI QWIPs. Under these conditions, responsivities of 1.7 mA/W are achieved at a dark-current density of 1.4 μA/cm^2, which compares well to the figures reported for state-of-the-art SiGe QWIPs in literature [16–18]. A comparison of the QWIPs demonstrated here to the latter reveals an additional fact: Up to now, none of the reported SiGe QWIPs have performed as expected from a straight-forward adaption of III-V design concepts to the SiGe system, using HH states instead of electron states. The SiGe QWIP spectra found in literature are either dominated by transitions between HH and LH/split-off states due to various reasons and therefore strong in TE polarization [17,18]. Or they are bias-dependent in a more complex way due to a design for tunable multi-color detection [16,27]. But up to now no clean adaption of a III-V QWIP design based on a HH1-HH2 transition strong in TM polarization has been experimentally demonstrated. In contrast, the SiGe QWIPs reported here exhibit a clear all-HH-based bound-to-continuum behavior with the associated peak shape and polarization dependence. Contributions by HH-LH transitions play only a minor role in the responsivity of our QWIPs as seen in Fig. 3(b), and show a significant contribution only in a clearly separated wavelength range. Therefore, we can report on the demonstration not only of a SiGe QWIP on sSOI, but also on a SiGe QWIP dominantly based on HH intersubband transitions.

The realized sSOI QWIP operates in a wavelength regime, in which the buried oxide of the sSOI substrate is extremely lossy. Our work therefore demonstrates, that competitive performance of sSOI-based devices can be achieved even in this spectral region by employing substrates with sufficiently thin silicon oxide layers. On the other hand, the presented sSOI QWIP concept can be

easily adapted for smaller wavelengths below 3.6 μm. In this regime, approaches for mid-infrared waveguiding based on micrometer-thick buried oxides are considered suitable [36], supporting the adaption of waveguide and resonator concepts commonly employed for Si photonic platforms in the near-infrared.

To conclude, the realized SiGe QWIPs demonstrate the large potential of sSOI as substrate material for group-IV based optoelectronic devices. For the sSOI system, the combination of photonic platform concepts established on silicon-on-insulator (SOI) with strain-balanced growth of SiGe-based devices operating in the mid-infrared is within reach. The results presented here on sSOI QWIPs therefore pave the way to a CMOS-compatible optoelectronic platform for novel on-chip sensing and detection functionalities in the spectral fingerprint regime of the mid-infrared.

References

1. P. Chaisakul, D. Marris-Morini, J. Frigerio, D. Chrastina, M.-S. Rouifed, S. Cecchi, P. Crozat, G. Isella, and L. Vivien, "Integrated germanium optical interconnects on silicon substrates," Nat. Photonics **8**(6), 482–488 (2014).
2. K. Debnath, F. Y. Gardes, A. P. Knights, G. T. Reed, T. F. Krauss, and L. O'Faolain, "Dielectric waveguide vertically coupled to all-silicon photodiodes operating at telecommunication wavelengths," Appl. Phys. Lett. **102**(17), 171106 (2013).
3. B. Stern, X. Zhu, C. P. Chen, L. D. Tzuang, J. Cardenas, K. Bergman, and M. Lipson, "On-chip mode-division multiplexing switch," Optica **2**(6), 530–535 (2015).
4. D. J. Moss, R. Morandotti, A. L. Gaeta, and M. Lipson, "New CMOS-compatible platforms based on silicon nitride and Hydex for nonlinear optics," Nat. Photonics **7**(8), 597–607 (2013).
5. D. C. S. Dumas, K. Gallacher, S. Rhead, M. Myronov, D. R. Leadley, and D. J. Paul, "Ge/SiGe quantum confined Stark effect electro-absorption modulation with low voltage swing at $\lambda = 1550$ nm," Opt. Express **22**(16), 19284–19292 (2014).
6. P. Rauter, L. Spindlberger, F. Schäffler, T. Fromherz, J. Freund, and M. Brehm, "Room-Temperature Group-IV LED Based on Defect-Enhanced Ge Quantum Dots," ACS Photonics **5**(2), 431–438 (2018).
7. M. Schatzl, F. Hackl, M. Glaser, P. Rauter, M. Brehm, L. Spindlberger, A. Simbula, M. Galli, T. Fromherz, and F. Schäffler, "Enhanced Telecom Emission from Single Group-IV Quantum Dots by Precise CMOS-Compatible Positioning in Photonic Crystal Cavities," ACS Photonics **4**(3), 665–673 (2017).
8. M. Grydlik, F. Hackl, H. Groiss, M. Glaser, A. Halilovic, T. Fromherz, W. Jantsch, F. Schäffler, and M. Brehm, "Lasing from Glassy Ge Quantum Dots in Crystalline Si," ACS Photonics **3**(2), 298–303 (2016).
9. S. Wirths, R. Geiger, N. von den Driesch, G. Mussler, T. Stoica, S. Mantl, Z. Ikonic, M. Luysberg, S. Chiussi, J. M. Hartmann, H. Sigg, J. Faist, D. Buca, and D. Grützmacher, "Lasing in direct-bandgap GeSn alloy grown on Si," Nat. Photonics **9**(2), 88–92 (2015).
10. M. Passoni, D. Gerace, L. O'Faolain, and L. C. Andreani, "Optimizing band-edge slow light in silicon-on-insulator waveguide gratings," Opt. Express **26**(7), 8470 (2018).
11. G. Roelkens, U. Dave, A. Gassenq, N. Hattasan, C. Hu, B. Kuyken, F. Leo, A. Malik, M. Muneeb, E. Ryckeboer, D. Sanchez, S. Uvin, R. Wang, Z. Hens, R. Baets, Y. Shimura, F. Gencarelli, B. Vincent, R. Loo, J. Van Campenhout, L. Cerutti, J.-B. Rodriguez, E. Tournie, X. Chen, M. Nedeljkovic, G. Mashanovich, L. Shen, N. Healy, A. C. Peacock, X. Liu, R. Osgood, and W. M. J. Green, "Silicon-Based Photonic Integration Beyond the Telecommunication Wavelength Range," IEEE J. Sel. Top. Quantum Electron. **20**(4), 394–404 (2014).
12. Y.-C. Chang, P. Wägli, V. Paeder, A. Homsy, L. Hvozdara, P. van der Wal, J. Di Francesco, N. F. de Rooij, and H. Peter Herzig, "Cocaine detection by a mid-infrared waveguide integrated with a microfluidic chip," Lab Chip **12**(17), 3020–3023 (2012).
13. M. Yu, Y. Okawachi, A. G. Griffith, N. Picqué, M. Lipson, and A. L. Gaeta, "Silicon-chip-based mid-infrared dual-comb spectroscopy," Nat. Commun. **9**(1), 6–11 (2018).
14. P. Biagioni, J. Frigerio, A. Samarelli, K. Gallacher, L. Baldassarre, E. Sakat, E. Calandrini, R. W. Millar, V. Giliberti, G. Isella, D. J. Paul, and M. Ortolani, "Group-IV midinfrared plasmonics," J. Nanophotonics **9**(1), 093789 (2015).

15. L. Baldassarre, E. Sakat, J. Frigerio, A. Samarelli, K. Gallacher, E. Calandrini, G. Isella, D. J. Paul, M. Ortolani, and P. Biagioni, "Midinfrared Plasmon-Enhanced Spectroscopy with Germanium Antennas on Silicon Substrates," Nano Lett. **15**(11), 7225–7231 (2015).

16. P. Rauter, T. Fromherz, G. Bauer, L. Diehl, G. Dehlinger, H. Sigg, D. Grützmacher, and H. Schneider, "Voltage-tunable, two-band mid-infrared detection based on Si/SiGe quantum-cascade injector structures," Appl. Phys. Lett. **83**(19), 3879–3881 (2003).

17. H. Durmaz, P. Sookchoo, X. Cui, R. Jacobson, D. E. Savage, M. G. Lagally, and R. Paiella, "SiGe Nanomembrane Quantum-Well Infrared Photodetectors," ACS Photonics **3**(10), 1978–1985 (2016).

18. P. Kruck, M. Helm, T. Fromherz, G. Bauer, J. F. Nützel, and G. Abstreiter, "Medium-wavelength, normal-incidence, p-type Si/SiGe quantum well infrared photodetector with background limited performance up to 85 K," Appl. Phys. Lett. **69**(22), 3372–3374 (1996).

19. P. Rauter, T. Fromherz, G. Bauer, N. Q. Vinh, B. N. Murdin, J. P. Phillips, C. R. Pidgeon, L. Diehl, G. Dehlinger, and D. Grützmacher, "Direct monitoring of the excited state population in biased SiGe valence band quantum wells by femtosecond resolved photocurrent experiments," Appl. Phys. Lett. **89**(21), 211111 (2006).

20. G. Dehlinger, L. Diehl, U. Gennser, H. Sigg, J. Faist, K. Ensslin, D. Grützmacher, and E. Müller, "Intersubband electroluminescence from silicon-based quantum cascade structures," Science **290**(5500), 2277–2280 (2000).

21. L. Diehl, S. Menteşe, E. Müller, D. Grützmacher, H. Sigg, U. Gennser, I. Sagnes, Y. Campidelli, O. Kermarrec, D. Bensahel, and J. Faist, "Electroluminescence from strain-compensated Si0.2Ge0.8/Si quantum-cascade structures based on a bound-to-continuum transition," Appl. Phys. Lett. **81**(25), 4700–4702 (2002).

22. G. Z. Mashanovich, M. M. Milošević, M. Nedeljkovic, N. Owens, B. Xiong, E. J. Teo, and Y. Hu, "Low loss silicon waveguides for the mid-infrared," Opt. Express **19**(8), 7112–7119 (2011).

23. W. Li, P. Anantha, S. Bao, K. H. Lee, X. Guo, T. Hu, L. Zhang, H. Wang, R. Soref, and C. S. Tan, "Germanium-on-silicon nitride waveguides for mid-infrared integrated photonics," Appl. Phys. Lett. **109**(24), 241101 (2016).

24. M. Brun, P. Labeye, G. Grand, J.-M. Hartmann, F. Boulila, M. Carras, and S. Nicoletti, "Low loss SiGe graded index waveguides for mid-IR applications," Opt. Express **22**(1), 508–518 (2014).

25. V. Vakarin, W. N. Ye, J. M. Ramírez, Q. Liu, J. Frigerio, A. Ballabio, G. Isella, L. Vivien, C. Alonso-Ramos, P. Cheben, and D. Marris-Morini, "Ultra-wideband Ge-rich silicon germanium mid-infrared polarization rotator with mode hybridization flattening," Opt. Express **27**(7), 9838–9847 (2019).

26. A. Malik, M. Muneeb, S. Pathak, Y. Shimura, J. Van Campenhout, R. Loo, and G. Roelkens, "Germanium-on-silicon mid-infrared arrayed waveguide grating multiplexers," IEEE Photonics Technol. Lett. **25**(18), 1805–1808 (2013).

27. P. Rauter, T. Fromherz, C. Falub, D. Grützmacher, and G. Bauer, "SiGe quantum well infrared photodetectors on pseudosubstrate," Appl. Phys. Lett. **94**(8), 081115 (2009).

28. S. Cecchi, E. Gatti, D. Chrastina, J. Frigerio, E. Müller Gubler, D. J. Paul, M. Guzzi, and G. Isella, "Thin SiGe virtual substrates for Ge heterostructures integration on silicon," J. Appl. Phys. **115**(9), 093502 (2014).

29. T. A. Langdo, M. T. Currie, Z. Y. Cheng, J. G. Fiorenza, M. Erdtmann, G. Braithwaite, C. W. Leitz, C. J. Vineis, J. A. Carlin, A. Lochtefeld, M. T. Bulsara, I. Lauer, D. A. Antoniadis, and M. Somerville, "Strained Si on insulator technology: From materials to devices," Solid-State Electron. **48**(8), 1357–1367 (2004).

30. G. Isella, D. Chrastina, B. Rössner, T. Hackbarth, H. J. Herzog, U. König, and H. von Känel, "Low-energy plasma-enhanced chemical vapor deposition for strained Si and Ge heterostructures and devices," Solid-State Electron. **48**(8), 1317–1323 (2004).

31. J. P. Dismukes, L. Ekstrom, E. F. Steigmeier, I. Kudman, and D. S. Beers, "Thermal and electrical properties of heavily doped Ge-Si alloys up to 1300°K," J. Appl. Phys. **35**(10), 2899–2907 (1964).

32. J. E. Ayers, "The measurement of threading dislocation densities in semiconductor crystals by X-ray diffraction," J. Cryst. Growth **135**(1-2), 71–77 (1994).

33. M. A. Moram and M. E. Vickers, "X-ray diffraction of III-nitrides," Rep. Prog. Phys. **72**(3), 036502 (2009).

34. T. Fromherz, E. Koppensteiner, M. Helm, G. Bauer, J. F. Nützel, and G. Abstreiter, "Hole energy levels and intersubband absorption in modulation-doped Si/Si1-xGex multiple quantum wells," Phys. Rev. B **50**(20), 15073–15085 (1994).

35. B. F. Levine, "Quantum-well infrared photodetectors," J. Appl. Phys. **74**(8), R1–R81 (1993).

36. R. A. Soref, S. J. Emelett, and W. R. Buchwald, "Silicon waveguided components for the long-wave infrared region," J. Opt. A: Pure Appl. Opt. **8**(10), 840–848 (2006).

37. P. Rauter, G. Mussler, D. Grützmacher, and T. Fromherz, "Tensile strained SiGe quantum well infrared photodetectors based on a light-hole ground state," Appl. Phys. Lett. **98**(21), 211106 (2011).